### Title

AC Plasmas Directly Excited in Liquid-Phase Hydrocarbons for H2 and Unsaturated C2 Hydrocarbon Production.




### Authors

Lim, Norleakvisoth

McFarland, Eric

Gordon, Mike



### Publication Date

2024-12-20

### DOI

10.1021/jacs.4c11174

Peer reviewed

JACS
JOURNAL OF THE AMERICAN CHEMICAL SOCIETY
pubs.acs.org/JACS



Article

# AC Plasmas Directly Excited in Liquid-Phase Hydrocarbons for $H_2$ and Unsaturated $C_2$ Hydrocarbon Production

Norleakvisoth Lim, Eric McFarland, and Michael J. Gordon*

Cite This: J. Am. Chem. Soc. 2025, 147, 397−408

Read Online

ACCESS | Metrics & More | Article Recommendations | Supporting Information

**ABSTRACT:** AC plasmas directly excited within liquid hydrocarbons were investigated for the production of hydrogen and unsaturated $C_2$ hydrocarbon in a recirculating liquid "jet" flow configuration. Arc discharges were excited at two different frequencies (60 Hz and 17.3 kHz) in $C_6$−$C_8$ hydrocarbons (hexane, cyclohexane, benzene, toluene, and xylene) to produce $H_2$, $C_2H_4$, $C_2H_2$, and $CH_4$, along with liquid and solid carbon byproducts. AC frequency was seen to modify the plasma properties and gas bubble formation dynamics, significantly influencing the efficiency and reaction pathway. Higher discharge frequency increased energy efficiency more than 2-fold by minimizing thermal losses and favored the production of hydrogenated compounds due to shorter reactant−plasma contact times. Further optimization of hexane conversion was achieved by introducing fluid flow around the plasma electrodes, which led to competitively low specific energy requirements (SERs) of 3.2 kWh/kg $C_2H_4$, 4.9 kWh/kg $C_2H_2$, and 24.3 kWh/kg $H_2$. The effect of hydrocarbon feed chemistry was analyzed, showing that hexane and cyclohexane are preferable for $C_2$ hydrocarbon syntheses, whereas aromatic hydrocarbons produce more $H_2$. Gas bubble dynamics and liquid/solid products were analyzed using high-speed imaging, optical emission spectroscopy (OES), gas chromatography−mass spectrometry (GC-MS), scanning electron microscopy/transmission electron microscopy (SEM/TEM), and Raman spectroscopy. This work contributes to the understanding of plasma conversion mechanisms within liquids and demonstrates the potential for the energy-efficient transformation of hydrocarbons with plasma in unique reaction environments.

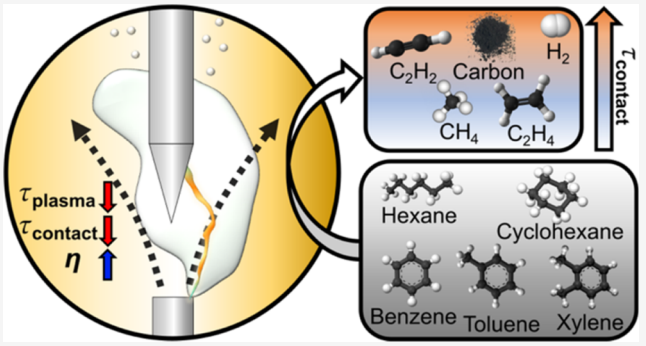


## 1. INTRODUCTION

While fossil resources remain available at low cost, new processes producing chemicals and clean fuels without releasing $CO_2$ can help reduce the economic barrier to our inevitable energy transition. More efficient pathways for transforming hydrocarbons into hydrogen and other valuable products without the emission of $CO_2$ are therefore of widespread interest. As early as 1931, the Shell Chemical Company produced hydrogen commercially via thermal decomposition (pyrolysis) of natural gas for ammonia production. The heat required for the endothermic decomposition was provided by natural gas combustion. Pyrolysis of hydrocarbons using electricity or emission-free hydrogen combustion has emerged as a potential interim method to produce hydrogen that might become an important energy carrier and clean fuel if produced at a low cost without greenhouse gas emissions.[1] Numerous recent studies have investigated the potential for natural gas and methane pyrolysis for hydrogen production in large-scale facilities ultimately using emission-free heat sources;[2,3] however, none have been shown to be cost-competitive to date.

Investigations of hydrocarbon cracking have extended beyond methane to other hydrocarbon gases and even liquids such as gasoline and diesel for onboard production of hydrogen. The latter seek to address challenges in the transportation and onboard utilization of hydrogen, as well as hydrogen's lower energy density (10 MJ/m$^3$ at 1 bar and <10 GJ/m$^3$ in liquid state at 20 K) compared to conventional fuels such as gasoline (>33 GJ/m$^3$).[4] The potential of generating value-added light hydrocarbons, $C_2H_2$ and $C_2H_4$, and hydrogen from heavy oil, reformates, and organics such as benzene, toluene, and hexane has also been demonstrated.[5−13]

Both nonthermal and thermal plasmas have been investigated for applications in chemical conversion.[14−21] Nonthermal plasmas generate active species at low temperatures, which makes new kinetic pathways and improved product selectivity possible in some cases. Thermal plasmas operate at thermal equilibrium and can easily achieve gas temperatures

Received: August 14, 2024
Revised: November 29, 2024
Accepted: December 5, 2024
Published: December 20, 2024

exceeding 3000 K. Moreover, the localized nature, inhomogeneity, and high reaction rates in thermal (arc) plasmas often allow the efficient and selective production of chemicals in ways that cannot be achieved with conventional thermal or thermocatalytic reactors. In the early 1800s, John Dalton demonstrated hydrogen production by direct methane decomposition using an electrical discharge.[14,22] Plasma-based decomposition of methane and gas phase light hydrocarbons in thermal arcs was even practiced commercially via the "Hüels" process.[23] The desired $C_2H_2$ product, an intermediate species in methane pyrolysis, was stabilized by rapid quenching of the product gas through water spray injection. A commercial facility based on the plasma-assisted "Kvaerner process" has also recently become operational to produce carbon black and hydrogen.[24] Similarly, Fulcheri et al. utilized a three-phase AC arc reactor to decompose methane into carbon black and $H_2$, achieving high conversion (>95%) and $H_2$ yield (~99%).[25] Other studies have explored plasma-based decomposition of gasified hydrocarbons, including *n*-hexane, cyclohexane, benzene, toluene, *n*-heptane, gasoline, diesel, kerosene, and heavy oils,[5,7,10,11,26−28] using DC/AC arcs, gliding arc discharges (GAD), as well as RF, microwave, and dielectric barrier discharges (DBD). These studies primarily focused on plasma-based decomposition (i.e., oxygen-free reforming) in gaseous media involving liquid hydrocarbon feeds that are vaporized before injection into the plasma zone or mixed with hot carrier gases generated by thermal plasmas.

Direct discharges in liquids, however, can offer several advantages, including smaller and more compact reactor designs due to the higher density of liquids and higher production rates. As early as 1945, the mechanisms of electrical discharges in liquids were examined by high-speed photography and time-dependent electrical power measurements by Komelkov.[29] Despite the early interest, there are few studies focused on chemical production from direct discharges in liquid hydrocarbons.[9,13,30−32] The formation of mass and thermal boundary layers at the gas−liquid interface can facilitate the quenching and stabilization of intermediate species, which can be used to tailor product selectivity. For the situation of transforming liquid hydrocarbons, a direct, in-liquid discharge can be more energetically efficient as it reduces the need to preheat carrier gases. Moreover, an in-liquid discharge creates a unique multiphase environment consisting of liquid reactant, plasma (reactive medium), gaseous products, and solid carbons, potentially simplifying downstream separation processes.

In this work, we explore the use of low current (<100 mA) AC arcs at two different frequencies (60 Hz and 17.3 kHz) to generate plasmas to decompose and reform various $C_6$−$C_8$ hydrocarbon liquids into $H_2$, unsaturated $C_2$, higher molecular weight hydrocarbons, and solid, separable carbon. A recirculating liquid jet reactor, shown in Figure 1, with online carbon filtration, was devised to improve mixing, prevent carbon bridge formation between plasma electrodes, and separate the solid carbon product. The impacts of AC excitation frequency and liquid recirculation rate on gaseous product distribution, production rates, and specific energy requirements (SER) for $C_2$ hydrocarbons and $H_2$ were evaluated. Our investigations included experiments with liquid hexane, cyclohexane, benzene, toluene, and xylene. Liquid reaction products were examined using gas chromatography−mass spectrometry (GC-MS) and solid carbon was characterized using Raman spectroscopy, scanning electron microscopy (SEM), and transmission electron microscopy (TEM).

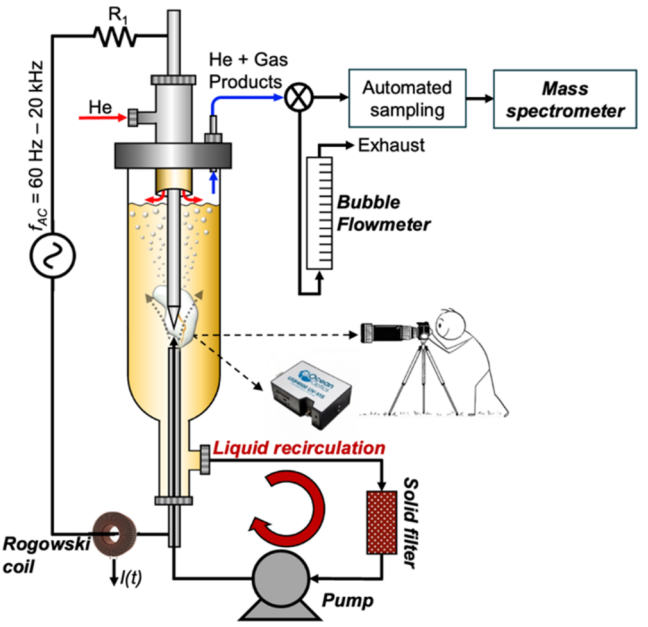


**Figure 1.** Schematic of the recirculating liquid jet plasma reactor and experimental setup.

## 2. EXPERIMENTAL METHODOLOGY

**2.1. Reactor Design.** The recirculating semibatch (plasma) reactor used in this study, Figure 1, consisted of a cylindrical glass tube (25.4 mm outer diameter and 20.6 mm inner diameter) with tapered tee connection at one end and an O-ring sealed Ultra-Torr fitting at the other. Hydrocarbon (HC) liquid was withdrawn from the tee side port of the reactor through a solids filter and delivered in an upward jet configuration through a 3.2 mm (1/8″) stainless-steel tube from the bottom of the reactor using a standard car fuel pump (38 GPH). The stainless-steel tube functioned as the ground electrode for the plasma and the HV counter electrode was a 3.2 mm (1/8″) diameter pointed titanium rod with O-ring seal. Helium (10 sccm) was injected into the headspace above the HC liquid surface as an internal mass spectrometry standard for quantitative measurement of product gas flow rates. The liquid recirculation loop served three functions, namely to remove carbon particles from the liquid, mix the liquid reaction medium, and eliminate carbon deposition on the electrodes which would otherwise form a conducting bridge and extinguish the plasma.

**2.2. Plasma Source and Characterization.** The plasma was driven with two separate AC sources (60 Hz and 5−20 kHz) with a ballast resistor (R1) in series. For 60 Hz, the output of a 140 V variable transformer was stepped up to 18 kV using a neon light transformer (Jefferson Transformer No. 721−111). The plasma current and voltage were controlled by varying the voltage output of the variable transformer. At higher frequencies (5−20 kHz), the sinewave output of a Fluke PM5138A function generator was amplified by an AE Techron 7780 amplifier and subsequently stepped up through a transformer cascade (Minipuls 4 GBS Elektronik GmbH), which could generate up to 40 kVpp. The ballast resistors used for low- and high-frequency operations were 750 and 50 Ω, respectively. A Tektronix P6015 high-voltage probe and a Pearson 411 current transformer (Rogowski coil) were used to measure the transient voltage and current. Optical emission spectra were captured using an Ocean Optics USB 4000 spectrometer with spectral intensity calibration performed against an Ocean Optics LS-1-CAL calibration light source. The integration time of the spectrometer was 25 ms. Movies of the plasma in operation were recorded using an acA640−


https://doi.org/10.1021/jacs.4c11174
J. Am. Chem. Soc. 2025, 147, 397−408

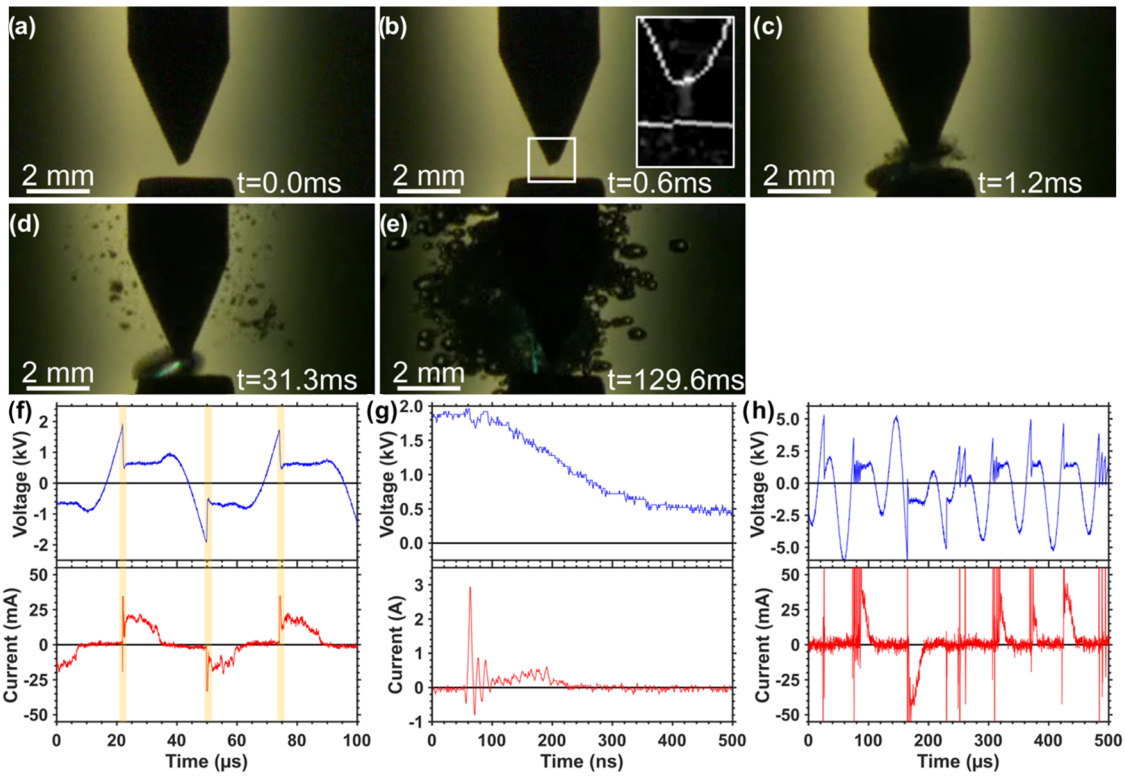


**Figure 2.** Temporal evolution of discharges in liquid hexane at 17.3 kHz. (a, c) Initial discharge progression in liquid hexane at 17.3 kHz. The inset in (b) shows the difference in pixel intensity between (b) and (a) to highlight streamer formation in liquid before the appearance of microbubbles. (e) Representation of plasma discharge in liquid hexane at 17.3 kHz. The pixel resolution of the images is 37 $\mu$m per pixel. Voltage and current characteristics of the corresponding discharge (f, g) without flow and (h) with flow through the electrodes. (g) Representation of the electrical transients during partial discharges (yellow shaded regions in (f)).

750uc Basler camera at 1628 frames per second (FPS) and 59 $\mu$s exposure time.

The average input power to the plasma was calculated as shown below:

$$P_{avg} = \frac{\int_0^T I(t)\cdot V(t)\mathrm{d}t}{T} \quad (1)$$

where $P_{avg}$, $T$, $I(t)$, and $V(t)$ are average power, period of a cycle, current, and voltage at time $t$, respectively. The current and voltage transients were recorded throughout the experiments and were then used to calculate an overall average power input.

**2.3. Experimental Conditions and Gas Product Analyses.** To quantify the gas production rate in each experiment, 10 sccm He was introduced into the gas headspace of the reactor, serving both as an internal reference and a carrier gas for vapor or gas products to the exhaust. The product gas composition was quantified using a specially designed automatic mass spectrometer sampling system detailed elsewhere.[33] The product gas was sampled every 2 min by first trapping a small gas sample into a known volume, expanding the sample into another chamber to 3−4 Torr total pressure, and then leaking the low-pressure sample into ultrahigh vacuum (UHV) for analysis using a Stanford Research Systems (SRS) RGA 100 mass spectrometer. Further details regarding the mass spectrometry measurement can be found in Supporting Information SI1. In addition, the total volumetric flow rate was measured at 30 s intervals throughout the experiments using a bubble flowmeter to corroborate with volumetric flow rates determined from mass spectrometry.

Each experimental trial lasted for a duration of 16 min with a recirculation rate or fluid velocity through the tube of 246 cm/s unless specified otherwise. Product compositions and production rates were determined by averaging measurements taken 5 min after plasma initiation in the liquid to ensure the system reached a mass transport steady state for rate measurements. Careful consideration was given to reactor design to minimize dead volume in the system and associated mixing issues to prevent underestimation of the production rate.

The product distribution or mole fraction, defined in eq 2, calculated in this study only considers the dominant gas phase products, such as $H_2$, $CH_4$, $C_2H_2$, and $C_2H_4$. The specific energy requirement (SER) to produce species $i$ is determined based on eq 3.

$$x_i = \frac{F_i}{\sum_{i=H_2,CH_4,C_2H_2,C_2H_4} F_i} \quad (2)$$

$$\mathrm{SER}_i = \frac{P_{avg}}{M_i F_i} \quad (3)$$

where $x_i$, $F_i$, and $M_i$ are mole fraction, molar flow rate, and molecular weight of species $i$, respectively.

**2.4. Liquid and Solid Product Analyses.** Products formed in the liquid reactant were analyzed by GC-MS (Waters GCT Premier GC TOF, which utilizes an Agilent 7890 A gas chromatograph and Agilent 7683 B autosampler). The liquid samples were mixed in a 1:1 ratio with hexane. Measurements were taken at 4 min for most hydrocarbons and at 6 min for xylene to prevent saturation of the GC detector by solvents and reactants. Peaks associated with initial hydrocarbon reactants appear below 4 min. Compound identification for each peak was performed using mass fragments with reference to the NIST database.

The carbon product was examined using SEM (Thermo Fisher Scientific Apreo C at 5 kV/0.1 nA), TEM (Thermo Scientific Talos F200X), and Raman spectroscopy (Horiba Jobin Yvon Xplora Plus spectrometer with 532 nm excitation). For TEM sample preparation, the carbon products were dispersed and diluted in methanol and sonicated for 30 min. The dispersed carbons were then cast onto a TEM grid (Electron Microscopy Sciences LC200-CU-UL). Raman sample preparation involved dispersing carbons in hexane and casting


https://doi.org/10.1021/jacs.4c11174
J. Am. Chem. Soc. 2025, 147, 397−408

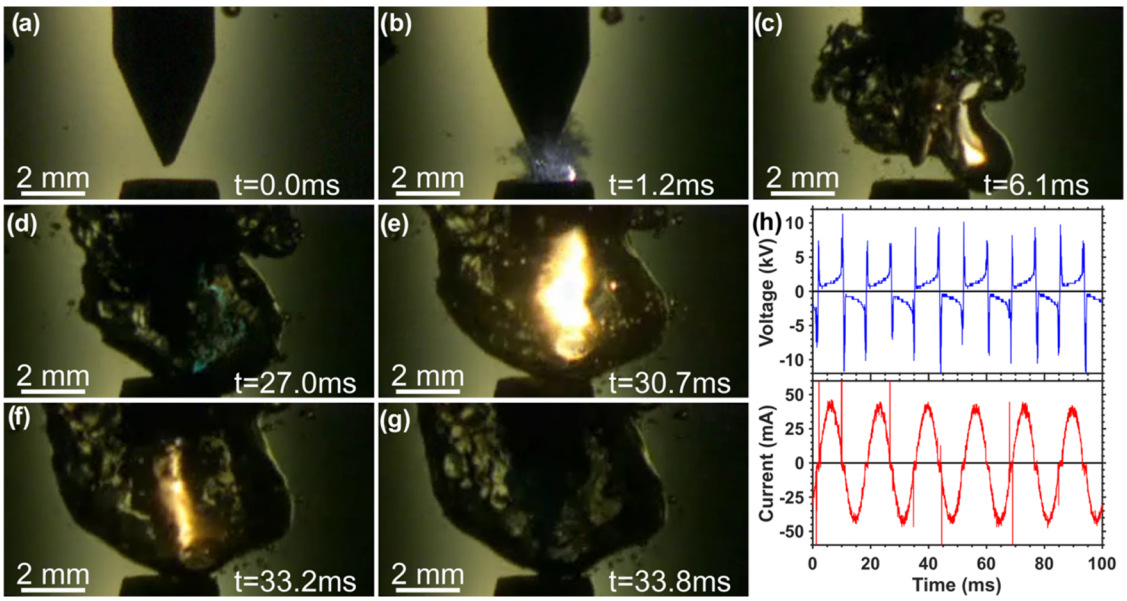


**Figure 3.** Temporal evolution of discharges in liquid hexane at 60 Hz. Time series images (a–c) show an initial discharge at 60 Hz and (d–g) demonstrate a typical continuous discharge during a half 60 Hz cycle (~8.3 ms). The pixel resolution of the images is 37 $\mu$m per pixel. (h) Voltage and current characteristics of discharges at 60 Hz.

them onto glass slides. In both cases, the samples were dried in a vacuum oven at 50 °C for 20 min and stored under vacuum overnight.

**2.5. Chemicals.** Liquid hydrocarbons used in this study were (mixed) hexanes (>98.5%, Fischer Chemical), cyclohexane (>99.5%, Tokyo Chemical Industry), benzene (>99%, Millipore), toluene (>99.5%, Fischer Chemical), and (mixed) xylenes (MP Biomedical).

## 3. RESULTS AND DISCUSSION

**3.1. Influence of Frequency on Hexane Dissociation in Arc Discharges.** Chemical conversion via plasma relies on the interplay between charge, mass, and energy transport in the system. Tuning the discharge duration can influence this transport, which, in turn, alters product selectivity and efficiency. To examine this relationship, the production rates and product distributions of direct discharges in liquid hydrocarbon were investigated using two distinct power sources at 17.3 kHz and 60 Hz frequencies. It should be noted that each half cycle has the potential to generate a single discharge pulse for an AC source, which means that the repetition rate of discharge pulses can be twice as high as the AC frequency. Hexane was chosen as the model liquid hydrocarbon in this study. The fluid was recirculated through the ground electrode at a velocity of 246 cm/s (8.9 mL/s) estimated at the tube outlet.

Figure 2 shows a time series of images of AC arc discharges in hexane at 17.3 kHz, along with the corresponding current and voltage transients. The images show that the discharge initiates via streamer formation extending from the HV electrode to the perimeter of the hollow ground electrode, resulting in microbubble formation, as depicted in Figure 2a–c. The structure and progression of the streamer could not be resolved due to the limiting time and spatial resolution of the imaging system. However, it is generally accepted that streamer discharges in liquid begin in the gaseous phase within microbubbles residing atop the electrode surface for discharges lasting microseconds or longer.[34] Korobeinukov et al. have demonstrated that these bubbles can deform along the electric field with streamers often emerging from their tips.[35] During the absence of pre-existing bubbles, they observed formations of heterogeneous structures near the electrode, a result of bubble formation from heating near the tip of the electrode before streamer formation. The streamer channel formed in liquid hydrocarbons has been suggested to be gaseous in nature, resulting in the formation of microbubbles after the discharge has dissipated.[35,36] These bubbles near the electrodes can further facilitate subsequent streamer discharges and an eventual transition to stable arc discharges, as shown in Figure 2d,e. The current and voltage waveforms of the stable arc discharges in Figure 2f show that there are two regimes, similar to AC discharges in the gas phase.[33] The first regime consists of intermittent and partial discharges that last for tens of nanoseconds, which are characterized by a sudden decrease in voltage and a sharp rise in current that can reach up to >3 A, as demonstrated in Figure 2g. The power input associated with this type of partial discharge is negligible compared to the power input of the arc discharge that subsequently forms. The discharge then transitions to a stable arc that lasts for 10 to 25 $\mu$s. When fluid flow is introduced through the ground electrode, it leads to an increase in partial discharges and irregular discharge patterns, as demonstrated by the current and voltage transients in Figure 2h. Although the distance between the two electrodes is ~0.4 mm, the arc length can fluctuate, depending on the surrounding hydrodynamic conditions. The discharge typically starts from the tip of the HV electrode and moves along its lateral surface as depicted in Figure 2d,e. This dynamic is influenced by the removal of bubbles away from the electrodes, driven by buoyant force and forced convection generated by the recirculation flow from the ground electrode.

Figure 3 illustrates the dynamic and electrical characteristics of a low-frequency (60 Hz) discharge. Similar to high-frequency (17.3 kHz) discharges, the plasma appears to initiate at the tip of the HV electrode with an intense discharge and progress along the lateral surface, as depicted in Figure 3a–c. Discharges tend to develop within the bubble created from prior discharges, often forming in areas near the HV


https://doi.org/10.1021/jacs.4c11174
J. Am. Chem. Soc. 2025, 147, 397–408

electrode tip that are enclosed by the bubble. Figure 3d–g shows the development of a single arc discharge over a half AC cycle. Initially, the arc appears to have an optical emission similar to that of a high-frequency discharge, as depicted in Figure 3d. As the discharge progresses, the emission becomes dominated by blackbody emission from soot particles. Figure 3h shows that the 60 Hz AC arc has a sawtooth-like voltage waveform, characterized by an increase in the voltage magnitude during the progression of each discharge. This indicates an increase in plasma impedance and thus an increase in arc length during each discharge, similar to that of a gliding arc discharge. Each bubble grows to an effective diameter of 5 to 8 mm and persists around the electrode region for up to 1.5 AC cycles (~25 ms) before being fully swept away by convection. In contrast, the bubbles produced at high frequency appear to collapse more suddenly, producing smaller bubbles on the order of micrometers to submillimeters, which moved away from the active area more swiftly.

The optical emission spectra of AC discharges in hexane indicate the presence of H, CH, and $C_2$ species, as shown in Figure 4. The emission from the high-frequency discharge is

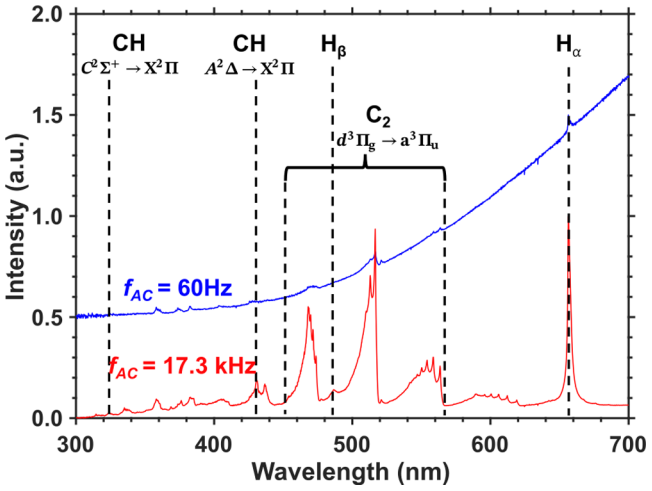


**Figure 4.** Comparison of optical emission spectra from 60 Hz and 17.3 kHz AC discharges in hexane. The experiment was carried out at a fluid jet velocity of 246 cm/s. The data presented are the average of spectra accumulated over a 50 s period. The optical spectral intensity of the 60 Hz discharge is offset by a value of 0.5 for clearer presentation.

mainly associated with the $C_2$ Swan bands due to the electronic transitions from $d^3\prod_g$ to $a^3\prod_u$. The $\Delta v = -2, -1, 0, 1$, and 2 sequences are observed with their corresponding band heads at 619.1, 563.5, 516.6, 473.7, and 438.1 nm, respectively. The emission lines at 656.6 and 486.5 nm are associated with the H-$\alpha$ and H-$\beta$ lines from atomic hydrogen. Ro-vibrational lines for CH at 314.5 and 431.0 nm associated with the $C^2\sum^+ \rightarrow X^2\Pi$ and $A^2\Delta \rightarrow X^2\Pi$ transitions are also observed. There are some unresolved peaks that lie between 300 and 400 nm that may be associated with CH, ionized carbon, and potentially Fe species. Using the $C_2$ Swan bands, the vibrational temperature of molecules in the high-frequency discharge was estimated to be 4000–5000 K under the assumption of local thermal equilibrium (LTE). Further information on the vibrational temperature estimation is detailed in Supporting Information SI2. The low-frequency discharge, on the other hand, is dominated by blackbody emission from soot particles that are formed from hexane decomposition. The estimated temperature from the blackbody emission was 2280 ± 150 K.

To further explore the differences between low- and high-frequency AC discharges, we used mass spectrometry to analyze the product gases, as shown in Figure 5. The peak currents were maintained at 40 mA for low-frequency discharges and 20–50 mA for high-frequency discharges. Figure 5a,b demonstrates changes in partial pressures of the exhaust gases before and during AC arc discharges at 60 Hz and 17.3 kHz frequencies, respectively. The mass spectra show that $H_2$, $CH_4$, $C_2H_2$, and $C_2H_4$ are the dominant gaseous products in both discharges. Additionally, trace amounts of $C_3$ and $C_4$ hydrocarbons were detected, with mass fragments spanning from 36 to 52 amu (or $m/z$), as shown in Supporting Information SI3. However, they constitute less than 3% of the gaseous products and are, therefore, neglected from further quantitative analyses.

Thermal dissociation or cracking of hydrocarbons is generally understood to initiate with C–C bond fission to create radical species.[37] In the case of *n*-hexane, the initial dissociation of a single molecule can yield either two $C_3H_7$ radicals or a combination of $C_2H_5$ and $C_4H_9$ radicals.[37,38] The path toward ethyl radical generation is significantly more favorable. These radicals then promote further dissociation of *n*-hexane through abstraction reactions, primarily involving ethyl, methyl, and hydrogen radicals, which leads to the production of $H_2$, $CH_4$, and $C_2H_6$, as well as various isomers of hexyl radical. Subsequently, these hexyl radicals dissociate through $\beta$-scission reactions to form a lighter alkene and other radicals, including $CH_3$, $C_2H_5$, $C_3H_7$, and $C_4H_9$. The propyl and butyl radicals can further dissociate into methyl and ethyl radicals or form unsaturated $C_3$–$C_4$ hydrocarbon products. Ultimately, the dissociation of *n*-hexane generates gaseous products such as $H_2$, ethylene, acetylene, and $C_3$–$C_4$ unsaturated hydrocarbons.[38] The dissociation of hexane in a 60 Hz AC discharge is expected to behave most similarly to thermal cracking due to its operation near or at thermal equilibrium. Based on mass spectrometry measurements in Figure 5a,c, the dominant hydrocarbon products from a 60 Hz discharge are $C_2H_2$, followed by $C_2H_4$ and $CH_4$, with minimal quantities of $C_3$–$C_4$ hydrocarbons. Yasunaga et al. examined high-temperature dissociation of *n*-hexane between 1000 and 1500 K in single-pulse shock tube experiments,[39] and found that dissociation indeed produces heavier hydrocarbons such as propane, propene, propyne, 1-butene, 1,3 butadiene, 1,2-butadiene, and 1-buten-3-yne. The concentrations of these $C_{3+}$ products decrease drastically above 1200 K, while $CH_4$, $C_2H_4$, and $C_2H_2$ were seen to increase with the temperature. This trend agrees with the product distribution of the 60 Hz discharge, as the gas temperature is certainly above 2000 K.

Compared to low-frequency AC arcs, the 17.3 kHz AC discharge favors the formation of more hydrogenated products, as evidenced by increased $C_2H_4$ and $CH_4$ mole fractions and decreased $H_2$ and $C_2H_2$ mole fractions. The higher-frequency discharge produces less carbon, as supported by the reduced continuum background emissions from soot particles, shown in Figure 4. This suggests that the two discharges may have distinct reaction pathways. The differences stem from variations in plasma properties and the effective residence time within the plasma region. As previously discussed, the high-frequency discharge generates much smaller bubbles that quickly move away from the plasma region, resulting in shorter


https://doi.org/10.1021/jacs.4c11174
J. Am. Chem. Soc. 2025, 147, 397–408

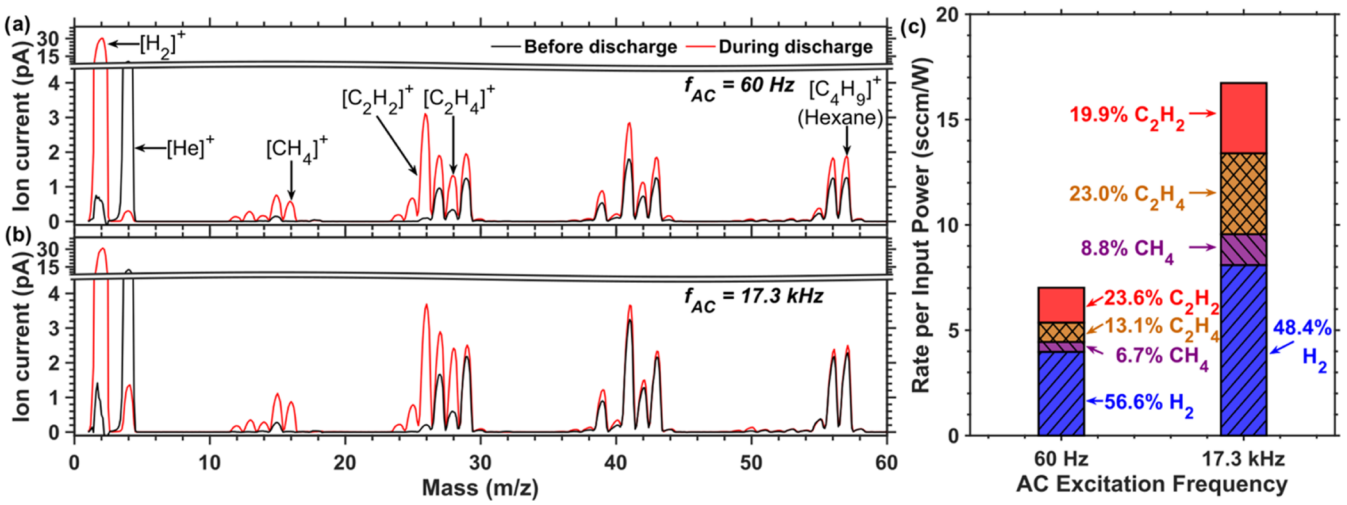


**Figure 5.** Product distributions and efficiencies of low- and high-frequency discharges. Comparative mass spectra of exhaust gases from before and during AC discharges at (a) 60 Hz and (b) 17.3 kHz. The signal peaks associated with the parent peaks of each species are annotated, except for hexane. The most intense daughter ion peak, $[C_4H_9]^+$, for hexane is shown instead of the less intense parent peak at $m/z$ = 86. (c) Power-normalized production rates for gases from AC discharges at 60 Hz and 17.3 kHz. The product distribution or mole fraction of the gaseous products is labeled. The experiments were carried out with a fluid velocity of 246 cm/s through the hollow ground electrode in both cases.

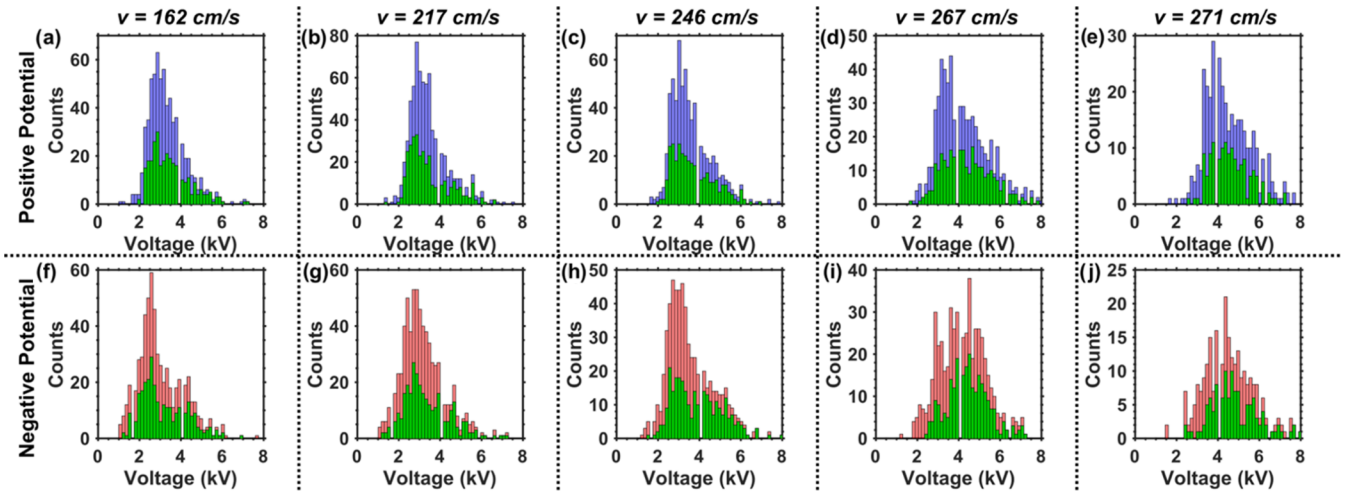


**Figure 6.** Influence of recirculation rate on the breakdown voltage of AC arc discharges. The distributions shaded in green show breakdown events that successfully led to subsequent arc discharges.

contact times. This shorter effective residence time explains the preference toward hydrogenated products, as increased contact time with the discharge leads to further dissociation of more saturated products, such as $CH_4$ and $C_2H_4$.

The gas production rates for 60 Hz and 17.3 kHz discharges were 279 and 73 sccm, with corresponding input powers of 39 and 4.2 W, respectively. The lower input power for the high-frequency discharge results from its lower duty cycle, as shown in Figure 2h. When the production rates are normalized by input power, demonstrated in Figure 5c, the high-frequency discharge proves to be more efficient, evidenced by its higher normalized production rates shown in Figure 5c. The change in hexane partial pressure in the exhaust gas was analyzed to examine the difference in efficiency between the two discharges. Initially, the hexane partial pressure was close to its vapor pressure, limited by the convective mass transport rate in the system. As the discharge progresses, the hexane partial pressure increases, which indicates that a fraction of the energy input contributes to thermal heating of the liquid reactant. The partial pressures of hexane increase by 49% for the low-frequency discharge and 9% for the high-frequency discharge. This suggests that higher-frequency discharges minimize thermal losses. Further investigation shows that at least 17% of the input power contributes to thermal loss in a high-frequency discharge. This is estimated from the temperature change in liquid hexane during a discharge, which serves as an underestimate of the actual thermal loss. Detailed energy balance and modeling are provided in Supporting Information SI4.

Discharge frequency significantly influences both the process efficiency and product distribution. Tuning the frequency can alter the plasma properties along with the surrounding bubble dynamics, which, in turn, affects the reactant contact time with the discharge. It has been demonstrated that the size of a bubble produced by a discharge increases proportionally to the energy input of the discharge[40] and the collapse time of the bubbles is dependent on their size.[41] Considering each bubble as a microreactor, the residence time can be effectively


https://doi.org/10.1021/jacs.4c11174
J. Am. Chem. Soc. 2025, 147, 397−408

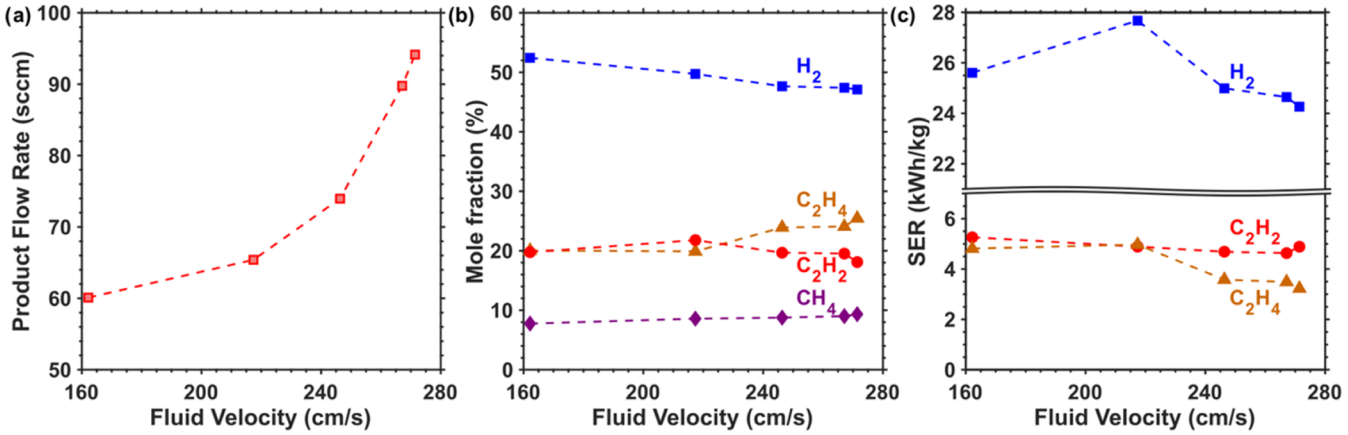


**Figure 7.** Influence of fluid velocity on plasma reactivity in liquid hexane. (a) Gas production rate increases with an increase in fluid velocity. Dependence of (b) product distribution and (c) specific energy requirement (SER) for $H_2$, $C_2H_2$, and $C_2H_4$ production on fluid velocity. The AC discharge was excited at 17.3 kHz.

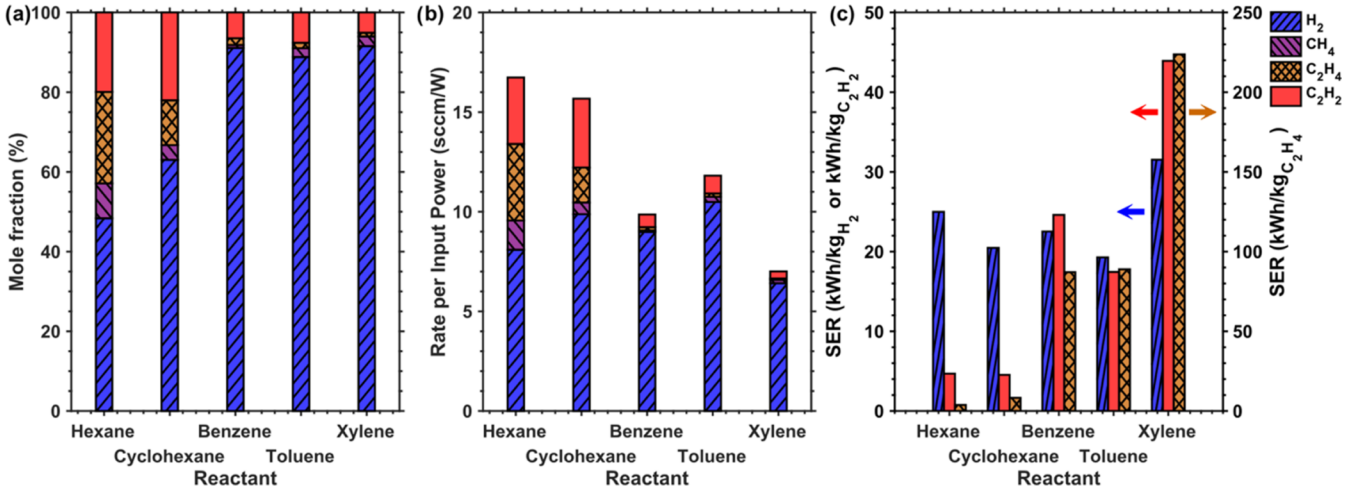


**Figure 8.** Dependence of (a) gas product distributions, (b) production rates, and (c) specific energy requirements for $H_2$, $C_2H_2$, and $C_2H_4$ on hydrocarbon reactants. The experiments were carried out at a 17.3 kHz AC frequency and 246 cm/s jet velocity.

controlled by varying the energy input, frequency, and pulse duration of the discharge. In addition, the contact time may be further fine-tuned by introducing a flow field across the electrodes.

**3.2. Influence of Flow Field on High-Frequency Discharges.** The influence of effective residence time on the production rate and selectivity of AC arc discharges was analyzed by varying the fluid velocity across the electrode gap from 162 cm/s (6 mL/s) to 271 cm/s (10 mL/s). The discharges in liquid hexane were excited by a 17.3 kHz AC power source. Figure 6 shows the distributions of the breakdown voltage under negative and positive potentials at different fluid velocities. The distribution shaded in green demonstrates breakdown events that successfully initiate arc discharges. The distributions of the breakdown voltages do not follow a normal distribution. At a velocity of 162 cm/s, the asymmetric distributions peak at approximately 2.9 kV for positive and 2.6 kV for negative potentials, as shown in Figure 6a,f. The low success rate of arc formation around the distribution peaks suggests that most breakdown events occurring between 2.6 and 3.0 kV correspond to streamer formation in the liquid phase. These streamers propagate from the tip of the HV electrode to the perimeter of the ground electrode or vice versa, facilitated by microbubbles in the surrounding electrode regions. This is further corroborated in Figure 6c,h, where the distribution peaks shift toward higher voltages around 3.1 kV, as the velocity increases to 246 cm/s. This increase in breakdown voltage is attributed to an increase in bubble removal rate from the electrode region, which increases breakdown time lag and impedes discharge formation.[35,42] In addition, there is a second broader distribution centered at 4 kV, which may correspond to breakdown events in the gas phase inside the bubbles. This wide distribution, which spans from low to high breakdown voltages, suggests that the arc discharges traverse along the lateral surface of the HV tip electrode along with the bubbles. As the velocity increases further, the distribution continues to broaden and shift to higher voltages, as shown in Figure 6d,e,i,j.

The introduction of flow across the electrodes has an influence on both the reaction rates and the product distribution, as shown in Figure 7. The reaction rate increases with increasing flow velocity, as demonstrated in Figure 7a. This is attributed to the increase in arc length due to changes in bubble dynamics surrounding the discharge and enhanced mass transport due to forced convection. However, it is not


https://doi.org/10.1021/jacs.4c11174
J. Am. Chem. Soc. 2025, 147, 397−408

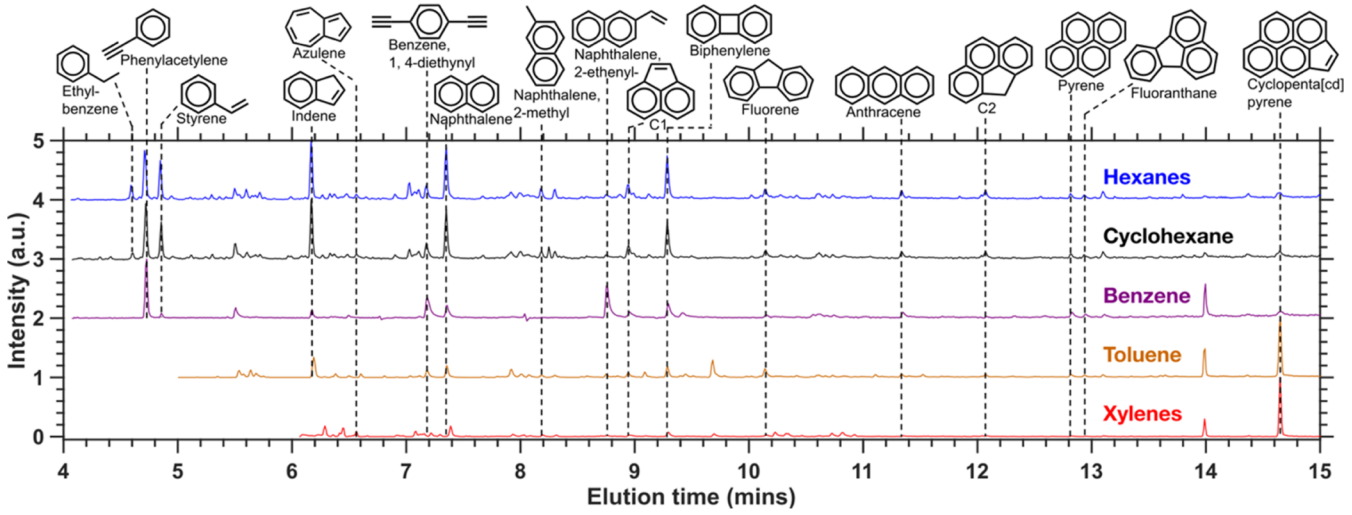


**Figure 9.** GC-MS analysis of liquid products from hydrocarbon conversions in 17.3 kHz AC discharges. The peaks labeled C1 and C2 are acenaphthylene and 4H-cyclopenta [def]phenanthrene, respectively.

possible to determine how much each factor contributes to the rate increase due to the difficulty in accurately measuring the arc lengths. In addition, the increase in flow velocity favors the formation of hydrogenated products, evidenced by increases in $C_2H_4$ and $CH_4$ mole fractions and decreases in $H_2$ and $C_2H_2$ mole fractions, as shown in Figure 7b. This behavior is similar to the transition from a low frequency to a higher-frequency discharge observed previously, which demonstrates that an increase in flow velocity reduces the effective residence time and impedes further dissociation of hydrocarbon products to $C_2H_2$ and carbon.

The change in flow velocity across the electrode gap affects the process efficiency and, thus, the SERs for the products. Specifically, the SER for $C_2H_4$ decreased from 4.8 to 3.2 kWh/kg $C_2H_4$ as flow increased from 161 to 271 cm/s, Figure 7c. Although the SER for $H_2$ and $C_2H_2$ inversely decreases with flow velocity as well, the changes are less significant. At a flow velocity of 271 cm/s, the SERs for $H_2$ and $C_2H_2$ were 24.3 kWh/kg of $H_2$ and 4.9 kWh/kg of $C_2H_2$, respectively. The significant improvement in energy efficiency for $C_2H_4$ production results from the benefit of increased production rates and improved selectivity for $C_2H_4$, whereas the efficiency of $C_2H_2$ production is reduced by a decrease in its selectivity. The energy required for both $C_2H_2$ and $C_2H_4$ production from hexane reforming via direct discharge in liquid is significantly lower than the reported values for plasma reforming in the gas phase,[7,28] the latter likely having input energy wasted in heating large carrier gas flows.

**3.3. Effect of Different Hydrocarbons.** In practical applications, hydrocarbon reforming utilizes light and heavy hydrocarbon feedstocks such as gasoline, naphtha, and other heavy crude oils, which consist of straight-chain alkanes, alkenes, cycloalkanes, and aromatics. To examine the influence of these different types of saturated and unsaturated hydrocarbons on the reactivity and product distribution, we analyzed and compared the dissociation of hexane, cyclohexane, benzene, toluene, and xylene. Figure 8 shows the dependence of product distribution and energy efficiency of hydrocarbon liquid reforming using a 17.3 kHz AC source.

Compared to hexane, the dissociation of cyclohexane produces more $H_2$, 63 mol %, and $C_2H_2$, 22 mol %, and less $C_2H_4$ and $CH_4$, as shown in Figure 8a. The initial dissociation of cyclohexane primarily occurs through C−C bond scission, instead of C−H bond dissociation, due to the lower C−C bond energies. This produces *n*-hexyl diradical and subsequently, 1-hexene, that further dissociate into allyl and propyl radicals.[43] These radicals eventually form $C_2H_4$, allene, propene, methyl, and H radicals. When there are sufficient radical concentrations, the dissociation of cyclohexane through abstraction reactions with methyl and hydrogen becomes more relevant, which leads to the production of $H_2$ and $CH_4$.[44] The production of acetylene mainly proceeds through the dissociation or abstraction of $C_2H_4$.[45] The pathways through which cyclohexane is converted into benzene, fused aromatic rings, and carbon remain an active research topic. However, the formation of aromatic compounds should generate more $H_2$ compared to $C_2$ hydrocarbon species. The increase in the selectivity for $H_2$ production in cyclohexane dissociation cannot be explained by the dissociation of $C_2H_4$ alone. This suggests that cyclohexane dissociation favors aromatic compounds and solid carbon formation compared to its straight-chain counterpart, hexane, under current process conditions.

In contrast to cyclohexane, the initial step for benzene dissociation occurs via C−H bond scission to form H and phenyl radicals.[46] In a low-temperature process, most of the product is biphenyl, which is formed through recombination of two phenyl radicals. At higher temperatures, the phenyl radical undergoes dehydrogenation reactions to form ortho-benzyne, which dissociates to $C_2H_2$ and $C_4H_2$.[47] The phenyl radical can form linear $C_6H_5$ through a bimolecular reaction and dissociates into the same products. Further formation of fused-ring compounds, such as naphthalene, occurs through a series of H abstraction and $C_2H_2$ addition (HACA) reactions starting with phenyl radicals.[48] These pathways align with the product distribution of benzene conversion observed in Figure 8a. The gaseous products primarily consist of $H_2$, 91 mol %, and $C_2H_2$, 6 mol %, with minor quantities of $C_2H_4$ and $CH_4$. Benzene conversion produces significantly more solid carbon products compared with hexane and cyclohexane. The addition of methyl groups to the aromatic molecule does not have a significant effect on the gaseous product composition, as evidenced in the conversion of toluene and xylene. There is


https://doi.org/10.1021/jacs.4c11174
J. Am. Chem. Soc. 2025, 147, 397−408

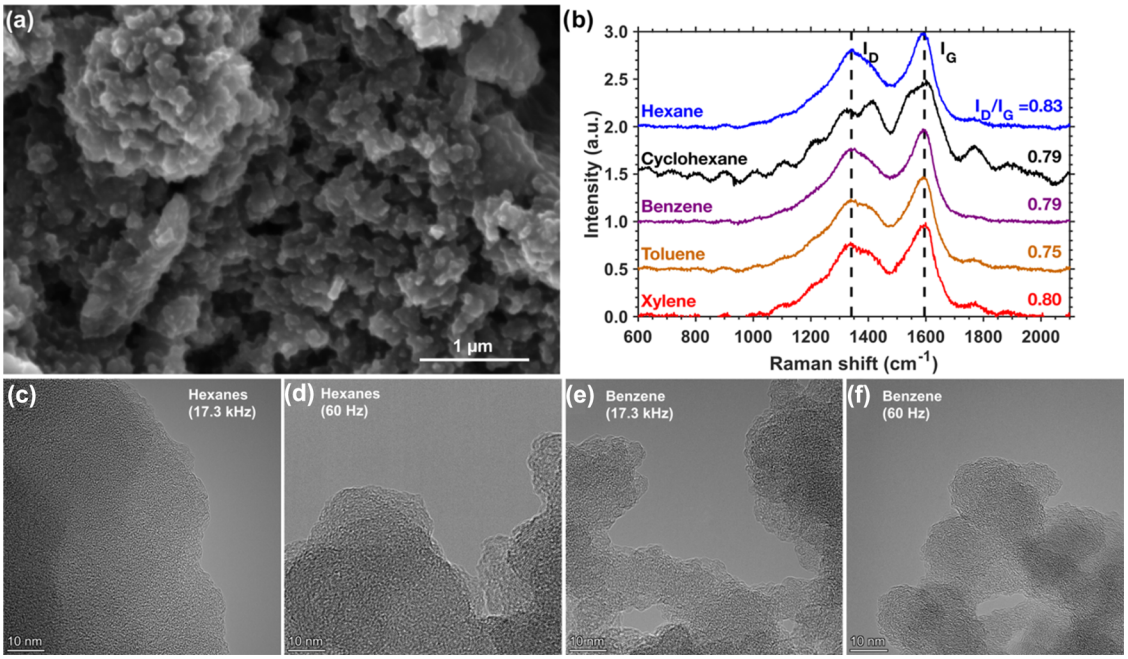


**Figure 10.** (a) Scanning electron micrograph of carbon products from liquid hexane. (b) Raman spectra of carbon products from the conversion of different hydrocarbons. The discharge was excited by a 60 Hz AC source for hexane and a 17.3 kHz AC source for the other hydrocarbons. (c–f) High-resolution transmission electron micrographs (HRTEM) of carbons from benzene and hexane dissociations through 60 Hz and 17.3 kHz AC discharges.

only a marginal increase in $CH_4$ production from these reactants.

In the high-frequency plasma, hexane has the highest conversion efficiency, as evidenced by the high normalized production rate in Figure 8b, followed by cyclohexane, toluene, benzene, and xylene. Similarly, Yan et al. investigated hydrocarbon pyrolysis using thermal plasma jets and concluded that *n*-hexane is the most reactive, with cyclohexane and toluene having sequentially lesser reactivities.[28] Figure 8c shows the energy required to produce $H_2$, $C_2H_2$, and $C_2H_4$ from liquid hydrocarbon conversion. Cyclohexane, benzene, and toluene show a lower SER for $H_2$ production, ranging from 19.3 kWh/kg $H_2$ to 22.5 kWh/kg $H_2$, which is due to their higher selectivity for $H_2$. The energy costs for $C_2H_2$ production are lowest for hexane and cyclohexane, which are 4.7 kWh/kg of $H_2$ and 4.5 kWh/kg of $C_2H_2$, respectively. Hexane is also the most efficient in producing $C_2H_4$, with an SER of 3.8 kWh/kg of $C_2H_4$. Xylene was observed to have the lowest energy efficiency for the production of $H_2$ and $C_2$ hydrocarbons.

The composition of the liquid products from hydrocarbon conversion was analyzed using GC-MS, as depicted in Figure 9. These products consist of substituted and fused aromatic rings, such as substituted benzenes, naphthalene, substituted naphthalenes, azulene, pyrene, anthracene, fluorene, fluoranthene, and cyclopenta[cd]pyrene. The presence of these aromatic molecules turns the liquid hydrocarbons from transparent to yellow due to ultraviolet (UV) light absorption. The UV–visible absorption spectrum of liquid products from hexane is shown in Supporting Information SI5. The conversions of hexane and cyclohexane yield similar product distributions in the liquid phase. This is likely because the primary reaction channel for cyclohexane dissociation generates straight-chain alkenes like 1-hexene. These alkenes subsequently undergo dissociation processes similar to those of other linear hydrocarbons. Hexane and cyclohexane conversion predominantly form naphthalene, indene, styrene, biphenylene, and phenylacetylene, which are important precursors for soot formation.

In the case of aromatic molecules, benzene dissociation primarily produces phenylacetylene with significantly lower concentrations of ethyl- and ethylene-substituted benzene compared to those of hexane and cyclohexane. These differences are due to the more direct route of benzene dissociation through ortho-benzyne to form acetylene, which then reacts with phenyl radicals to form phenylacetylene. In contrast, hexane and cyclohexane produce ethane, ethylene, and their respective radicals through abstraction and $\beta$-scission reactions, providing additional pathways for the formation of ethyl- and ethylene-substituted benzenes. Furthermore, benzene conversion also yielded more 2-ethynyl naphthalene and 1,4-diethynyl benzene. The dissociation of toluene and xylene produces significantly higher concentrations of fused-ring aromatics, such as cyclopenta[cd]pyrene, compared to the other hydrocarbons.

Figure 10a shows an SEM image of amorphous carbon produced from hexane conversion, which serves as a representation of carbon produced from the liquid hydrocarbons investigated in this work. These solids are composed of micrometer to submicron-sized aggregates. In the case of carbon produced from benzene, we observed even smaller, tens of nanometers-sized aggregates, confirmed by TEM images and dynamic light scattering (DLS). Raman spectral analysis between 600 and 2000 cm$^{-1}$ shows two prominent peaks at 1595 and 1340 cm$^{-1}$, which result from graphite layer in-plane vibrations (G peak) and the defect-assisted phonon mode (D peak), respectively.[49] The D-to-G peak intensity ratio serves as a qualitative indicator of the degree of graphitization of different carbons.[50] The Raman spectrum of amorphous carbon is shown in Figure 10b. It should be noted that the D and G peaks of carbon from hexane conversion in a 17.3


https://doi.org/10.1021/jacs.4c11174
J. Am. Chem. Soc. 2025, 147, 397–408

kHz discharge are overshadowed by the fluorescence background from aromatic molecules, shown in Supporting Information SI6. The Raman spectrum of carbon from hexane dissociation at 60 Hz is shown for comparison in Figure 10b instead. The spectra demonstrate that the amorphous carbon exhibits comparable graphitic qualities, as evidenced by their similar D and G peak intensities.

The carbon from hexane and benzene conversion in 17.3 kHz and 60 Hz discharges were further examined using HRTEM to evaluate the influence of hydrocarbon feed and discharge frequency on solid products, shown in Figure 10c–f. The carbon produced from hexane under high-frequency discharge was highly amorphous with little to no graphitic features, which may explain its low D and G peak intensities relative to the fluorescence background. In the lower-frequency discharge, the carbon becomes more graphitic, as evidenced by the short graphite flakes observed in Figure 10d. This is likely due to the longer residence time and the higher gas temperature associated with low-frequency discharges. In comparison, carbon from aromatic hydrocarbons like benzene under both low- and high-frequency discharges shows formations of aggregates with spherical-like features that are fused together. There are graphite flakes with concentric features within these spherical aggregates that resemble structures observed in carbon black.

**3.4. Perspective and Scalability.** To provide some perspective on the plasma conversion process in this study, one can examine the overall mass balance and cost for a prototypical situation involving a hexane-like feed. Using the gas production rates from Figure 8b for hexane dissociation under 17.3 kHz AC drive, and inferring the leftover nongaseous carbon species by difference (and assuming they can be approximated as solid carbon), the overall estimated reaction occurring is as follows:

$$3.14C_6H_{14}(l) \rightarrow 8H_2(g) + 3.75C_2H_4(g) + 3.5C_2H_2(g) + 1.5CH_4(g) + 2.86C(s) \quad (4)$$

Given the measured SER for $H_2$ in this reaction scenario (25 kWh/kg $H_2$, Figure 8c) and a nominal energy cost of electricity of \$0.10/kWh, the $H_2$ production cost would be \$0.005 per mole of $H_2$. This value is less than half of the energy required for electrolysis in practice (60 kWh/kg $H_2$[51]), which requires \$0.012 per mole of $H_2$ at a similar electricity cost. Moreover, the reaction in eq 4 generates value-added $C_2H_4$ (\$12–24/kmol[52]) and $C_2H_2$ (\$26–48/kmol[53]) products in addition to $H_2$ (\$10–20/kmol,[54] assuming current green $H_2$ costs). Thus, if implemented with a mixed $C_6$–$C_8$ naphtha feed (~\$60/kmol[55]) for \$13 of electrical energy input (\$127 kWh/kmol $C_6$ converted) and \$190 for the hydrocarbon feed (\$60/kmol), \$220-\$420 in product value is generated even if no value is assigned to the carbon and methane coproducts. Provided that a reasonable capital charge can be defended, the process could be economically viable. Optimizing the plasma process to produce specific desired products should therefore be explored as well as carrying out a detailed technoeconomic analysis to assess capital (CapEx) and operational expenditures (OpEx). We also note that eq 4 is oversimplified, and only provides a rough estimate of the reaction stoichiometry and that we neglect the formation of longer chain alkanes ($C_8$–$C_{25}$) that do indeed appear in the GC-MS data. As such, the theoretical energy input for the real process would be lower, as small amounts of these products (that we neglect) can contribute significantly to the overall process efficiency since their heats of formation are large and negative (−220 to −550 kJ/mol). Also, polymerization reactions, if they might also occur, tend to be exothermic with products having large, negative heats of formation, thus adding to potentially smaller overall heats of reaction as shown in eq 4.

To evaluate the scalability of such a plasma process, an upper limit on the active plasma (reactor) volume can be estimated from Figure 3e. Given the dimensions involved and assuming all the bubble volume around the electrodes as the active reactor volume, one can estimate an upper limit volume of ~0.13 $cm^3$ (6 mm diameter and 4.5 mm long cylinder). This plasma operating condition produced 160 sccm of $H_2$ or an equivalent of 0.007 mol of $H_2$/min. Given the aforementioned active volume, the production rate would be 1.8 kg of $H_2/m^3$, which is equivalent to 57 kilotons of $H_2$ per annum per $m^3$ (57 kta $H_2/m^3$). Thus, scaling the plasma volume to the order of 1 $m^3$ is not unrealistic given the ability to multiplex plasma electrodes or liquid jet flows.

## 4. SUMMARY

A recirculating flow, AC-excited liquid jet plasma reactor was developed to evaluate the feasibility of direct plasma reforming of liquid hydrocarbons to form $H_2$ and $C_2$ hydrocarbons at 60 Hz and 17.3 kHz. The system design facilitated mixing, prevented carbon bridge formation between the plasma electrodes, and allowed easy separation of solid carbon products. The dissociation of various liquid hydrocarbons (hexane, cyclohexane, benzene, toluene, and xylene) at low and high AC frequencies yielded primarily gaseous ($H_2$, $CH_4$, $C_2H_4$ and $C_2H_2$), and solid (carbon) products, with minor fractions of liquid products (naphthalene, substituted benzenes, indene, and other aromatic molecules). The low- and high-frequency discharges resulted in different plasma operating characteristics, discharge durations, and repetition rates, which altered gas bubble formation and dynamics around the plasma electrode region. As such, the effective reactant–plasma "contact time" or residence time could be sufficiently manipulated to modify the efficiency and reaction pathways for reforming. The energy efficiency of the reforming process was seen to more than double when the excitation frequency was changed from 60 Hz to 17.3 kHz, an effect likely attributed to less thermal loss to the surrounding liquid medium. In addition, the shorter contact time associated with a higher drive frequency favored more hydrogenated products such as $C_2H_4$ and $CH_4$.

The influence of the residence time was further examined independently from the discharge frequency by varying fluid flow velocity across the electrode gap. With higher flow velocity and shorter residence time, the selectivity for $C_2H_4$ increased, which resulted in a further decrease in the SER for $C_2H_4$. The lowest SER for $C_2H_4$ from hexane conversion achieved was 3.2 kWh/kg of $C_2H_4$, and those for $H_2$ and $C_2H_2$ were 24.3 kWh/kg of $H_2$ and 4.9 kWh/kg of $C_2H_2$, respectively. The energy efficiency achieved in the liquid discharges is lower than those reported in previous studies of similar hydrocarbons in gas phase plasma reforming; however, for the production of hydrogen, the measured SER was significantly lower than for water electrolysis (60 kWh/kg $H_2$ in practice).

The influence of liquid hydrocarbon feed composition on the product distribution and energy efficiency in high-frequency AC discharges showed that hexane and cyclohexane


https://doi.org/10.1021/jacs.4c11174
J. Am. Chem. Soc. 2025, 147, 397–408

had similar compositions of gaseous and liquid products consistent with their similar thermal dissociation pathways. The transition to aromatic hydrocarbons, such as benzene, toluene, and xylene, leads to a significant increase in selectivity for $H_2$. Overall, hexane and cyclohexane have a higher energy efficiency for producing ethylene and acetylene, whereas benzene and toluene can be more efficient in producing $H_2$. Xylene had the lowest energy efficiency to produce $H_2$, or $C_2$ hydrocarbons, which may be due to its low reaction rate.

Our experiments demonstrate the potential for direct plasma conversion of abundant, low-cost liquid hydrocarbon feedstocks to hydrogen and value-added chemical products. This plasma process could be economically realized with low-temperature, scalable reactors powered by low-emission electricity from renewable and nuclear sources during our energy transition.

## ■ ASSOCIATED CONTENT

### Supporting Information

The Supporting Information is available free of charge at https://pubs.acs.org/doi/10.1021/jacs.4c11174.

Mass spectrometry measurements; mass spectra fitting; vibrational temperature fitting; energy balances; and UV−vis absorption and fluorescence spectra (PDF)

## ■ AUTHOR INFORMATION


### Corresponding Author

**Michael J. Gordon** − *Department of Chemical Engineering, University of California, Santa Barbara, California 93106, United States;* orcid.org/0000-0003-0123-9649; Email: gordon@ucsb.edu

### Authors

**Norleakvisoth Lim** − *Department of Chemical Engineering, University of California, Santa Barbara, California 93106, United States*

**Eric McFarland** − *Department of Chemical Engineering, University of California, Santa Barbara, California 93106, United States*

Complete contact information is available at: https://pubs.acs.org/10.1021/jacs.4c11174



### Funding

This material was based upon work supported by the Robert G. Rinker Endowment for Chemical Engineering at UCSB, with auxiliary funding provided by C-Zero, Inc. and the National Science Foundation Graduate Research Fellowship under Grant No. 2139319.


### Notes

The authors declare no competing financial interest.

## ■ ACKNOWLEDGMENTS


The authors acknowledge the MRL Shared Experimental Facilities of UCSB supported by the MRSEC program (NSF DMR 1720256), a member of the Materials Research Facilities Network (www.mrfn.org).


## ■ REFERENCES


(1) Muradov, N.; Veziroglu, T. Green" Path from Fossil-Based to Hydrogen Economy: An Overview of Carbon-Neutral Technologies. *Int. J. Hydrogen Energy* **2008**, *33* (23), 6804−6839.

(2) Schneider, S.; Bajohr, S.; Graf, F.; Kolb, T. State of the Art of Hydrogen Production via Pyrolysis of Natural Gas. *ChemBioEng Rev.* **2020**, *7* (5), 150−158.

(3) Scapinello, M.; Delikonstantis, E.; Stefanidis, G. D. The Panorama of Plasma-Assisted Non-Oxidative Methane Reforming. *Chem. Eng. Process.: Process Intensif.* **2017**, *117*, 120−140.

(4) Tartakovsky, L.; Sheintuch, M. Fuel Reforming in Internal Combustion Engines. *Prog. Energy Combust. Sci.* **2018**, *67*, 88−114.

(5) Fan, Z.; Sun, H.; Dou, L.; Zhang, S.; Han, W.; Zhang, C.; Shao, T. One-Step High-Value Conversion of Heavy Oil into H2, C2H2 and Carbon Nanomaterials by Non-Thermal Plasma. *Chem. Eng. J.* **2023**, *461*, No. 141860.

(6) Liu, Y.; Dou, L.; Zhou, R.; Sun, H.; Fan, Z.; Zhang, C.; Ostrikov, K. K.; Shao, T. Liquid-Phase Methane Bubble Plasma Discharge for Heavy Oil Processing: Insights into Free Radicals-Induced Hydrogenation. *Energy Convers. Manage.* **2021**, *250*, No. 114896.

(7) Ma, J.; Zhang, M.; Wu, J.; Yang, Q.; Wen, G.; Su, B.; Ren, Q. Hydropyrolysis of N-Hexane and Toluene to Acetylene in Rotating-Arc Plasma. *Energies* **2017**, *10* (7), No. 899.

(8) Camerotto, E.; Schepper, P. D.; Nikiforov, A. Y.; Brems, S.; Shamiryan, D.; Boullart, W.; Leys, C.; Gendt, S. D. Study of Ultrasound-Assisted Radio-Frequency Plasma Discharges in n-Dodecane. *J. Phys. D: Appl. Phys.* **2012**, *45* (43), No. 435201.

(9) Averin, K. A.; Borisov, R. S.; Lebedev, Y. A. Microwave Discharge in Liquid Hydrocarbons: Study of a Liquid Hydrocarbon after Its Discharge Treatment Including Air Bubbling. *High Energy Chem.* **2020**, *54* (3), 210−216.

(10) Son, Y.-S.; Kim, J.; Choi, I.-Y.; Kim, J.-C. Decomposition of *n* -Hexane Using a Dielectric Barrier Discharge Plasma. *Environ. Technol.* **2021**, *42* (13), 2067−2076.

(11) Yan, J. H.; Bo, Z.; Li, X. D.; Du, C.. M.; Cen, K. F.; Chéron, B. G. Study of Mechanism for Hexane Decomposition with Gliding Arc Gas Discharge. *Plasma Chem. Plasma Process.* **2007**, *27* (2), 115−126.

(12) Chung, K.-H.; Lam, S. S.; Park, Y.-K.; Kim, S.-J.; Jung, S.-C. Application of Liquid-Phase Plasma for the Production of Hydrogen and Carbon from the Plasma-Induced Cracking of Liquid Hydrocarbons. *Fuel* **2022**, *328*, No. 125297.

(13) Titov, E. Y.; Bodrikov, I. V.; Vasiliev, A. L.; Kurskii, Y. A.; Ivanova, A. G.; Golovin, A. L.; Shirokov, D. A.; Titov, D. Y.; Bodrikova, E. R. Non-Thermal Plasma Pyrolysis of Fuel Oil in the Liquid Phase. *Energies* **2023**, *16* (10), No. 4017.

(14) Henry, W. XXVI. Experiments on Ammonia, and an Account of a New Method of Analyzing It, by Combustion with Oxygen and Other Gases; in a Letter to Humphry Davy, Esq. Sec. R. S. &c. from William Henry, M.D., F. R. S. V. P. of the Lit and Phil Society, and Physician to the Infirmary, at Manchester. *Philos. Trans. R. Soc.* **1809**, *99*, 430−449.

(15) Lee, D. H.; Kim, K.-T.; Song, Y.-H.; Kang, W. S.; Jo, S. Mapping Plasma Chemistry in Hydrocarbon Fuel Processing Processes. *Plasma Chem. Plasma Process.* **2013**, *33* (1), 249−269.

(16) Polak, L. Low-Temperature Plasma in Petroleum Chemistry. *Pet. Chem. U.S.S.R.* **1967**, *7* (2), 136−152.

(17) George, A.; Shen, B.; Craven, M.; Wang, Y.; Kang, D.; Wu, C.; Tu, X. A Review of Non-Thermal Plasma Technology: A Novel Solution for CO2 Conversion and Utilization. *Renewable Sustainable Energy Rev.* **2021**, *135*, No. 109702.

(18) Peng, P.; Chen, P.; Schiappacasse, C.; Zhou, N.; Anderson, E.; Chen, D.; Liu, J.; Cheng, Y.; Hatzenbeller, R.; Addy, M.; Zhang, Y.; Liu, Y.; Ruan, R. A Review on the Non-Thermal Plasma-Assisted Ammonia Synthesis Technologies. *J. Cleaner Prod.* **2018**, *177*, 597−609.

(19) Indarto, A.; Choi, J.-W.; Lee, H.; Song, H. K. Decomposition of Greenhouse Gases by Plasma. *Environ. Chem. Lett.* **2008**, *6* (4), 215−222.

(20) Gallagher, M. J.; Fridman, A. Plasma Reforming for H2-Rich Synthesis Gas. In *Fuel Cells: Technologies for Fuel Processing*; Elsevier, 2011; pp 223−259.

(21) Gomez, E.; Rani, D. A.; Cheeseman, C. R.; Deegan, D.; Wise, M.; Boccaccini, A. R. Thermal Plasma Technology for the Treatment

of Wastes: A Critical Review. *J. Hazard. Mater.* **2009**, *161* (2−3), 614−626.
(22) Dalton, J. *A New System of Chemical Philosophy*; Cambridge University Press: Manchester, England, 1808; Vol. *2*.
(23) Fincke, J. R.; Anderson, R. P.; Hyde, T.; Detering, B. A.; Wright, R.; Bewley, R. L.; Haggard, D. C.; Swank, W. D. Plasma Thermal Conversion of Methane to Acetylene. *Plasma Chem. Plasma Process.* **2002**, *22* (1), 105−136.
(24) Bolouri, K. S.; Amouroux, J. Reactor Design and Energy Concepts for a Plasma Process of Acetylene Black Production. *Plasma Chem. Plasma Process* **1986**, *6* (4), 335−348.
(25) Fulcheri, L.; Probst, N.; Flamant, G.; Fabry, F.; Grivei, E.; Bourrat, X. Plasma Processing: A Step towards the Production of New Grades of Carbon Black. *Carbon* **2002**, *40* (2), 169−176.
(26) Beiers, H.-G.; Baumann, H.; Bittner, D.; Klein, J.; Jüntgen, H. Pyrolysis of Some Gaseous and Liquid Hydrocarbons in Hydrogen Plasma. *Fuel* **1988**, *67* (7), 1012−1016.
(27) Hao, H.; Wu, B. S.; Yang, J.; Guo, Q.; Yang, Y.; Li, Y. W. Non-Thermal Plasma Enhanced Heavy Oil Upgrading. *Fuel* **2015**, *149*, 162−173.
(28) Yan, B.; Xu, P.; Li, X.; Guo, C. Y.; Jin, Y.; Cheng, Y. Experimental Study of Liquid Hydrocarbons Pyrolysis to Acetylene in H2/Ar Plasma. *Plasma Chem. Plasma Process.* **2012**, *32* (6), 1203−1214.
(29) Komelkov, V. S. Mechanism of the Pulsed Breakdown of Liquids. *Dokl AN SSSR* **1945**, *47*, 269−272.
(30) Malik, M. A.; Hughes, D.; Malik, A.; Xiao, S.; Schoenbach, K. H. Study of the Production of Hydrogen and Light Hydrocarbons by Spark Discharges in Diesel, Kerosene, Gasoline, and Methane. *Plasma Chem. Plasma Process.* **2013**, *33* (1), 271−279.
(31) Hamdan, A.; Liu, J. Scenario of Carbon-encapsulated Particle Synthesis by Spark Discharges in Liquid Hydrocarbons. *Plasma Process. Polym.* **2021**, *18* (7), No. 2100013.
(32) Saifutdinova, A. A.; Sofronitskiy, A. O.; Timerkaev, B. A.; Saifutdinov, A. I. Plasma-Chemical Decomposition of Hydrocarbons on the Basis of the Micro-Arc Discharge with Disc Electrodes Rotating in the Bulk of Raw Materials. *Russ. Phys. J.* **2020**, *62* (11), 2132−2136.
(33) Lim, N.; Wu, Y.; Gordon, M. J. Impact of Pressure and Hydrogen Dilution on the Kinetics of Methane Decomposition in AC-Excited, High Pressure Plasmas. *Plasma Chem. Plasma Process.* **2024**, *44* (1), 47−64.
(34) Sun, A.; Huo, C.; Zhuang, J. Formation Mechanism of Streamer Discharges in Liquids: A Review. *High Voltage* **2016**, *1* (2), 74−80.
(35) Korobeinikov, S. M.; Melekhov, A. V.; Besov, A. S. Breakdown Initiation in Water with the Aid of Bubbles. *High Temp.* **2002**, *40* (5), 652−659.
(36) Lesaint, O.; Gournay, P. On the Gaseous Nature of Positive Filamentary Streamers in Hydrocarbon Liquids. I: Influence of the Hydrostatic Pressure on the Propagation. *J. Phys. D: Appl. Phys.* **1994**, *27* (10), 2111−2116.
(37) Hunter, K. C.; East, A. L. L. Properties of C−C Bonds *in n* -Alkanes: Relevance to Cracking Mechanisms. *J. Phys. Chem. A* **2002**, *106* (7), 1346−1356.
(38) Randolph, K. L.; Dean, A. M. Hydrocarbon Fuel Effects in Solid-Oxide Fuel Cell Operation: An Experimental and Modeling Study of n-Hexane Pyrolysis. *Phys. Chem. Chem. Phys.* **2007**, *9* (31), 4245−4258.
(39) Yasunaga, K.; Yamada, H.; Oshita, H.; Hattori, K.; Hidaka, Y.; Curran, H. Pyrolysis of N-Pentane, n-Hexane and n-Heptane in a Single Pulse Shock Tube. *Combust. Flame* **2017**, *185*, 335−345.
(40) Hoffer, P.; Bílek, P.; Prukner, V.; Bonaventura, Z.; Šimek, M. Dynamics of Macro- and Micro-Bubbles Induced by Nanosecond Discharge in Liquid Water. *Plasma Sources Sci. Technol.* **2022**, *31* (1), No. 015005.
(41) Podbevšek, D.; Lokar, Ž.; Podobnikar, J.; Petkovšek, R.; Dular, M. Experimental Evaluation of Methodologies for Single Transient Cavitation Bubble Generation in Liquids. *Exp. Fluids* **2021**, *62* (8), No. 167.
(42) Bílek, P.; Tungli, J.; Hoder, T.; Šimek, M.; Bonaventura, Z. Electron−Neutral Bremsstrahlung Radiation Fingerprints the Initial Stage of Nanosecond Discharge in Liquid Water. *Plasma Sources Sci. Technol.* **2021**, *30* (4), No. 04LT01.
(43) Kiefer, J. H.; Gupte, K. S.; Harding, L. B.; Klippenstein, S. J. Shock Tube and Theory Investigation of Cyclohexane and 1-Hexene Decomposition. *J. Phys. Chem. A* **2009**, *113* (48), 13570−13583.
(44) Khandavilli, M. V.; Djokic, M.; Vermeire, F. H.; Carstensen, H.-H.; Van Geem, K. M.; Marin, G. B. Experimental and Kinetic Modeling Study of Cyclohexane Pyrolysis. *Energy Fuels* **2018**, *32* (6), 7153−7168.
(45) Steil, U.; Braun-Unkhoff, M.; Naumann, C.; Frank, P. In *Experimental Study of the Pyrolysis of Cyclohexane at Shock Tube Relevant Conditions*, Proceedings of the European Combustion Meeting; Institute of Combustion Technology: Louvain-la-Neuve, Belgium, 2005.
(46) Saggese, C.; Frassoldati, A.; Cuoci, A.; Faravelli, T.; Ranzi, E. A Wide Range Kinetic Modeling Study of Pyrolysis and Oxidation of Benzene. *Combust. Flame* **2013**, *160* (7), 1168−1190.
(47) Wang, H.; Laskin, A.; Moriarty, N. W.; Frenklach, M. On Unimolecular Decomposition of Phenyl Radical. *Proc. Combust. Inst.* **2000**, *28* (2), 1545−1555.
(48) *Soot Formation in Combustion: Mechanisms and Models*; Bockhorn, H.; Goldanskii, V. I.; Schäfer, F. P.; Toennies, J. P.; Lotsch, H. K. V., Eds.; Springer Berlin Heidelberg: Berlin, Heidelberg, 1994; Vol. *59*.
(49) Bokobza, L.; Bruneel, J.-L.; Couzi, M. Raman Spectroscopy as a Tool for the Analysis of Carbon-Based Materials (Highly Oriented Pyrolitic Graphite, Multilayer Graphene and Multiwall Carbon Nanotubes) and of Some of Their Elastomeric Composites. *Vib. Spectrosc.* **2014**, *74*, 57−63.
(50) Ferrari, A. C.; Robertson, J. Interpretation of Raman Spectra of Disordered and Amorphous Carbon. *Phys. Rev. B* **2000**, *61* (20), No. 14095.
(51) Fulcheri, L.; Rohani, V.-J.; Wyse, E.; Hardman, N.; Dames, E. An Energy-Efficient Plasma Methane Pyrolysis Process for High Yields of Carbon Black and Hydrogen. *Int. J. Hydrogen Energy* **2023**, *48* (8), 2920−2928.
(52) Ethylene Pricing Report 2024: Price Trend, Chart, Market Analysis, News, Demand, Historical and Forecast Data, Report ID: SR112024A22306 2024, IMARC Group. https://www.imarcgroup.com/ethylene-pricing-report (accessed August 12, 2024).
(53) Acetylene price trend and forecast, 2024. https://www.chemanalyst.com/Pricing-data/acetylene-21 (accessed August 12, 2024).
(54) Schelling, K. Green Hydrogen to Undercut Gray Sibling by End of Decade BloombergNEF, 2024. https://about.bnef.com/blog/green-hydrogen-to-undercut-gray-sibling-by-end-of-decade/ (accessed August 12, 2024).
(55) Naphtha Trading Economics, 2024. https://tradingeconomics.com/commodity/naphtha (accessed August 12, 2024).


https://doi.org/10.1021/jacs.4c11174
*J. Am. Chem. Soc.* 2025, 147, 397−408